



Effect of pore size on bone ingrowth into porous titanium implants fabricated by additive manufacturing: An *in vivo* experiment



Naoya Taniguchi^{a,*}, Shunsuke Fujibayashi^a, Mitsuru Takemoto^a, Kiyoyuki Sasaki^b, Bungo Otsuki^a, Takashi Nakamura^c, Tomiharu Matsushita^d, Tadashi Kokubo^d, Shuichi Matsuda^a

^a Department of Orthopaedic Surgery, Kyoto University Graduate School of Medicine, 54 Kawahara-cho, Shogoin, Sakyo, Kyoto 606-8507, Japan

^b Sagawa Printing Co., Ltd., 5-3, Inui, Morimoto-Cho, Mukou-Shi, Kyoto 617-8588, Japan

^c National Hospital Organization Kyoto Medical Center, 1-1, Mukaihatacho, Hukakusa, Hushimi, Kyoto 612-8555, Japan

^d Department of Biomedical Sciences, College of Life and Health Sciences, Chubu University, 1200 Matsumoto-cho, Kasugai, Aichi 487-8501, Japan

ARTICLE INFO

Article history:

Received 5 February 2015

Received in revised form 24 September 2015

Accepted 23 October 2015

Available online 28 October 2015

Keywords:

Selective laser melting

Porous titanium

Additive manufacturing

Pore size

Bone ingrowth

ABSTRACT

Selective laser melting (SLM) is an additive manufacturing technique with the ability to produce metallic scaffolds with accurately controlled pore size, porosity, and interconnectivity for orthopedic applications. However, the optimal pore structure of porous titanium manufactured by SLM remains unclear. In this study, we evaluated the effect of pore size with constant porosity on *in vivo* bone ingrowth in rabbits into porous titanium implants manufactured by SLM. Three porous titanium implants (with an intended porosity of 65% and pore sizes of 300, 600, and 900 μm , designated the P300, P600, and P900 implants, respectively) were manufactured by SLM. A diamond lattice was adapted as the basic structure. Their porous structures were evaluated and verified using microfocus X-ray computed tomography. Their bone–implant fixation ability was evaluated by their implantation as porous-surfaced titanium plates into the cortical bone of the rabbit tibia. Bone ingrowth was evaluated by their implantation as cylindrical porous titanium implants into the cancellous bone of the rabbit femur for 2, 4, and 8 weeks. The average pore sizes of the P300, P600, and P900 implants were 309, 632, and 956 μm , respectively. The P600 implant demonstrated a significantly higher fixation ability at 2 weeks than the other implants. After 4 weeks, all models had sufficiently high fixation ability in a detaching test. Bone ingrowth into the P300 implant was lower than into the other implants at 4 weeks. Because of its appropriate mechanical strength, high fixation ability, and rapid bone ingrowth, our results indicate that the pore structure of the P600 implant is a suitable porous structure for orthopedic implants manufactured by SLM.

© 2015 Elsevier B.V. All rights reserved.

1. Introduction

Titanium and its alloys are widely used in implants in the orthopedic and dental fields because of their high fracture resistance and biocompatibility. However, titanium itself is bioinert, and polished or abraded titanium has no bone-bonding ability [1]. Therefore, several techniques have been developed to give titanium an irregular surface to improve its fixation ability. For example, sintered bead-bonded, grit-blasted, and fiber mesh-bonded titanium are in clinical use for hip prostheses [2–5]. Besides conventional porous surface coatings on dense titanium, various methods have been developed to produce a porous titanium body [6]. These include sintering with powders [7,8], solid-state foaming by expansion of argon-filled pores [9], compressing and

sintering of titanium fibers [10], and polymeric sponge replication [11]. However, these methods cannot manufacture implants with a precisely controlled porosity and pore shape, size, and interconnectivity suitable for inducing tissue ingrowth, which anchors the prosthesis to the surrounding bone and prevents implant loosening.

Selective laser melting (SLM) [12–14] is a newly developed additive manufacturing (AM) process, in which a product is created by melting selected areas of powder layers using a computer-controlled laser beam. Because of its ability to build complicated three-dimensional (3D) shapes, AM has great potential to solve the problems of creating a porous surface coating on a dense titanium and porous titanium body. Recently, complicated shapes such as structures similar to human cancellous bone [15] and implant shape of joint arthroplasty [16] were manufactured by AM from metal powder. Moreover, bioactive treatments such as hydroxyapatite coating [17] and NaOH, HCl, and heat treatment [15] were verified to confer osteoconductivity on metal implants manufactured by AM. Moreover, in a model of cervical vertebral body replacement, porous metal implants manufactured by AM were implanted into anterior cervical defects in sheep by Yang et al. [18] and Wu et al. [19]. They reported that bone–implant stability

* Corresponding author at: 54 Kawahara-cho, Shogoin, Sakyo, Kyoto 606-8507, Japan.

E-mail addresses: tani110@kuhp.kyoto-u.ac.jp (N. Taniguchi),

shfuji@kuhp.kyoto-u.ac.jp (S. Fujibayashi), m.take@kuhp.kyoto-u.ac.jp (M. Takemoto),

kiy-sasaki@spcom.co.jp (K. Sasaki), bungo@kuhp.kyoto-u.ac.jp (B. Otsuki),

ntaka@kuhp.kyoto-u.ac.jp (T. Nakamura), matsushi@isc.chubu.ac.jp (T. Matsushita),

kokubo@isc.chubu.ac.jp (T. Kokubo), smat522@kuhp.kyoto-u.ac.jp (S. Matsuda).

was enhanced by bone ingrowth. Furthermore, Wu et al. [19] reported that porous metal showed higher mechanical bone–implant stability than a polyetheretherketone cage implanted with an autograft. These studies indicated the utility of AM for manufacturing cervical implants. However, the optimal pore structure for bone ingrowth into AM-manufactured porous titanium implants remains unclear.

To date, many studies have been conducted to investigate the influence of the porosity and pore size of porous materials on biological behavior [20]. However, the majority of these studies were based on experiments involving porous calcium phosphate. The biodegradability of calcium phosphate varies depending on parameters such as porosity, crystallinity, chemical purity, and surface roughness [21]. In particular, the pore size was verified to affect the resorption rate by theoretical approach [22]. Therefore, it is difficult to ensure the characteristic uniformity of experimental samples made from calcium phosphate and, in turn, difficult to determine the true effect of porous structure through experiments involving this material. In contrast, metal is unresorbable and its characteristics remain constant at a range of geometries, which confers experimental uniformity on a study. Therefore, from this perspective, porous metal is more suitable for investigating the effect of porous structure on biological behavior. However, few studies have used porous metal to investigate the influence of porous structures on biological behavior [6,23–25]. Using four types of porous titanium implant manufactured using a powder-sintering method, our groups [23] demonstrated that bone ingrowth is affected not only by porosity and pore size but also by interconnected pore throat size. Our groups concluded that pores with narrow throats are disadvantageous for bone formation. However, porous titanium manufactured by powder-sintering methods exhibits heterogeneity in terms of pore size and pore throat size [23]. Furthermore, conventional manufacturing techniques are incapable of separately controlling geometrical parameters related to pore structure. In this regard, AM is the most suitable method of producing samples for use in investigations of the effect of pore structure on biological behavior, because AM can manufacture well-interconnected porous metal implants and allows separate control of parameters related to pore structure.

Recently, two researchers began to take advantage of AM to study the effect of porous structure on biological behavior *in vitro* [26] and *in vivo* [27]. In an *in-vitro* study, Van Bael et al. [26] reported that the use of porous titanium implants manufactured using SLM with a pore size of 1000 μm yielded a significant increase in cell density and metabolic activity than the use of implants with a pore size of 500 μm . However, the *in vitro* environment differs greatly from the *in vivo* environment, in which the flow of nutrition and oxygen around the implants is constant. In an *in vivo* study, Van Der Stok et al. [27] examined the effect of inserting porous implants composed of the titanium alloy Ti6Al4V, which has two different porosities (68% and 88%) with the same pore size (490 μm), into cortical defects in rats. They observed good bone formation, and there was no significant difference in bone formation between the two porosities of the scaffold. On the other hand, the pore sizes examined in the model of cervical vertebral body replacement in sheep were 710 and 1100 μm for Wu et al. [19] and Yang et al. [18], respectively. Although both studies did not compare between different structures with respect to which porous structures induced high stabilization in the point that their porous implants induced enough bone for stabilization, consideration of their results is useful in the investigation of optimal porous structure. Accordingly, these four previous studies using AM demonstrate that AM-manufactured porous titanium implants with a pore size of 490–1100 μm exhibit a reasonable performance *in vivo*. However, to date, no reports have clarified the true effect of porous structure in terms of pore size and pore throat size at a constant porosity. Furthermore, the effect on the biological behavior of a pore size of less than 490 μm , which porous titanium implants manufactured by conventional methods often possesses [23,28], has yet to be examined in experiments using AM-manufactured porous titanium implants *in vivo*.

In this study, we investigated the effect of pore size on bone ingrowth using samples manufactured by AM, which allows the separate control of pore structure, to determine the optimal porous structure for metal implants manufactured by this process. Therefore, porous implants with three pore sizes (300, 600, and 900 μm) and with a constant porosity were manufactured using SLM. To characterize these implants, we conducted 3D structural analysis [23] using micro-focus X-ray computed tomography (micro-CT) and mechanical comprehension tests. Moreover, to evaluate biological performance, we conducted two *in vivo* experiments. First, we examined the fixation ability of each implant to bone by implanting plate-type implants into the cortical bone of the rabbit tibia. Second, we evaluated bone ingrowth into the pores of each implant using cylinder-type implants implanted into cancellous bone in the rabbit femur.

2. Materials and methods

2.1. Computer-aided design

The computer-aided design (CAD) was created using the software Magics (Materialise HQ, Leuven, Belgium). A diamond crystal lattice, in which each atom is tetrahedron-like and surrounded by four other atoms [29], was adapted as the basic form of the porous structure for the following two reasons. First, the diamond crystal lattice is composed of only dull angles (109.5). This is suitable for manufacture using SLM because sharp angles are often corrupted by adhesion to the nearby shaft in the melting phase. Second, the diamond crystal lattice remains stable under multidirectional compressive forces, even with high porosity; this confers high safety in clinical situations. A single unit of the diamond crystal lattice is shown in Fig. 1. As shown in Fig. 1, the cross-section of the pore throat is hexagonal.

The manufactured porous titanium implants were designed to have a porosity of 65%, with pore sizes of 300, 600, and 900 μm , and were designated the P300, P600, and P900 implants, respectively. A representative model is shown in Fig. 1.

2.2. Materials

In this study, gas-atomized, commercially pure titanium powder (Grade 2; Osaka Titanium Technologies Co., Ltd., Hyogo, Japan) with a particle size of <45 μm was used as the starting powder.

2.3. Selective laser melting

An SLM system (EOSINT-M270; Electro Optical Systems GmbH, Munich, Germany) was used for AM. The machine was equipped with a 200 W Yb fiber laser with a spot size of 100 μm . Porous titanium was manufactured using a laser power of 120 W and a laser scanning speed of 200 mm/s. The thickness of the powder layer was 30 μm , and the hatching distance was maintained at 120 μm . These parameters were determined by our previous study [15]. After the SLM process, the implants were heat-treated at 1300 $^{\circ}\text{C}$ for 1 h and allowed to cool naturally in the furnace in an argon atmosphere. The heat treatment was intended to sinter incompletely melted Ti particles at the surface and to prevent these particles from falling off. The heat treatment was detailed in previous reports [15,30].

According to the CAD, we manufactured porous titanium plates (15 \times 10 \times 2 mm; porous layer thickness: 1.8 mm, solid layer thickness: 0.2 mm) or cylinders covered with a thin lateral wall (diameter: 6 mm; length: 9 mm; lateral wall thickness: 0.2 mm) for animal experiments (Fig. 2). The lateral wall has intended two reasons. The first was to observe the longest distance possible in the limited space available in rabbits. The second was to maintain the maximum possible uniformity in experimental conditions at the bone–implant interface between implants. Furthermore, cubes (10 \times 10 \times 10 mm) for measurement of porosity and 3D structural analysis using micro-CT, and cylinders

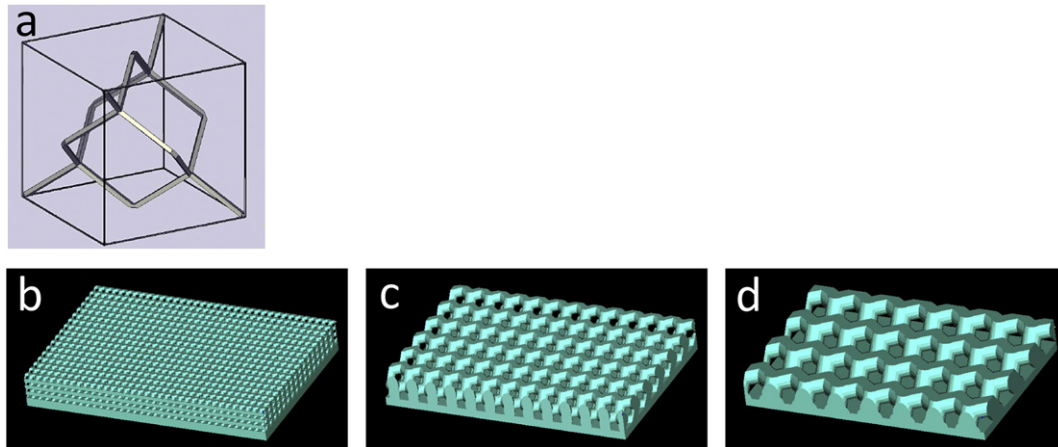


Fig. 1. Basic single unit and computer-aided design of porous-surfaced titanium plates with different pore sizes. a) A single unit of diamond crystal lattice; b) P300; c) P600; d) P900 (size: $15 \times 10 \times 2$ mm).

(diameter: 12 mm; length: 12 mm) for mechanical testing were manufactured. These four shapes of implants were manufactured using the three different porous structures described above (P300, P600, and P900) in sizes that were suitable to each analysis.

2.4. Characterization of the porous titanium implants

2.4.1. Porosity

The porosity of the samples was calculated from the weight and apparent volume of porous cubes ($10 \times 10 \times 10$ mm). All measurements were conducted at room temperature.

2.4.2. Microfocus X-ray computed tomography-based structural analysis

Micro-CT-based structural analysis was performed according to our previous studies [23,31]. Using a micro-CT system (SMX-100CT-SV3; Shimadzu Corporation, Kyoto, Japan, resolution

threshold of 33 LP/mm; accelerating voltage of 90 kV; a beam current of $40 \mu\text{A}$; filter of 0.5 mm Cu), we obtained reconstructed images consisting of $512 \times 512 \times 431$ voxels, with a voxel size of $(12.7 \mu\text{m})^3$. These images were processed with a combination of freeware (ImageJ; National Institutes of Health, Bethesda, MD, USA; <http://rsb.info.nih.gov/ij/>) and commercially available software (VGStudio MAX 2.2; Volume Graphics GmbH, Heidelberg, Germany). Before analysis, micro-CT images were converted to images consisting of $646 \times 646 \times 490$ voxels, yielding a voxel size of $(10 \mu\text{m})^3$. Next, we performed a segmentation process using the Adaptive 3D Threshold Plugin for ImageJ (C. Henden and J. Bache-Wiig; <http://www.pvv.org/~perchrh/imagej/>), and each image was converted to a binary image where the pixel population was assigned to either the foreground (material) or the background (pore). From these data, the pore size, pore throat size, material strut size, and specific surface area of each implant were calculated. Details of the 3D structural analysis are described in the following section.

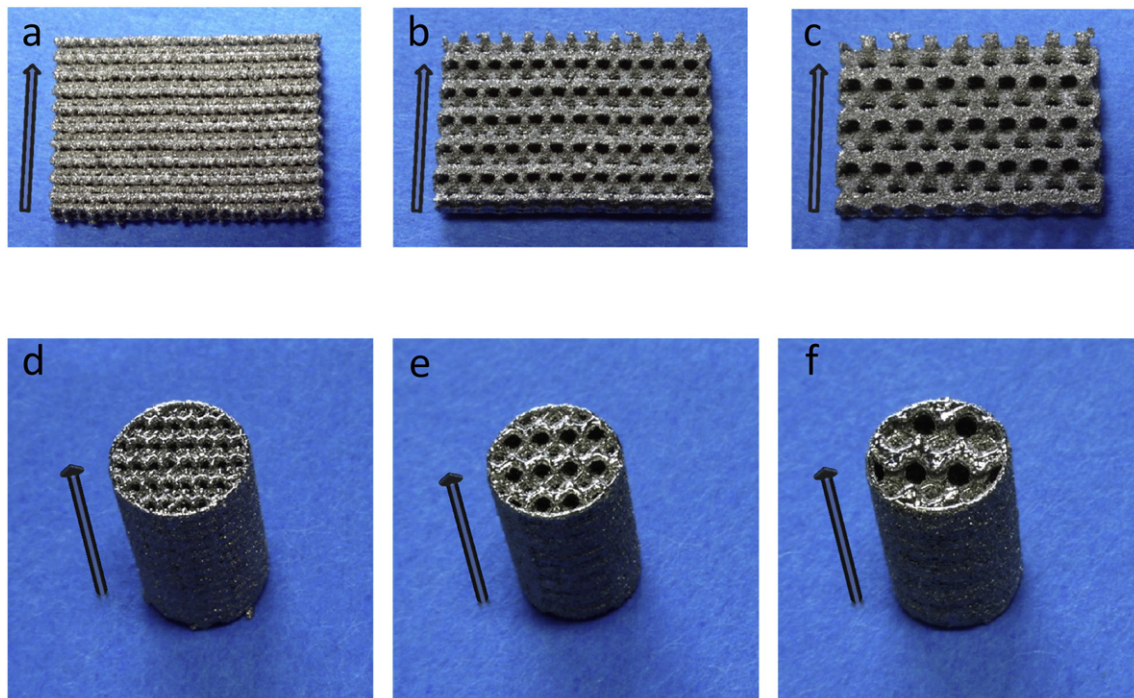


Fig. 2. Porous implants used in the in vivo animal experiments. a) P300, b) P600, and c) P900 porous-surfaced titanium plates (size: $15 \times 10 \times 2$ mm). d) P300, e) P600, and f) P900 porous cylinders covered with a thin lateral wall (size: diameter 6 mm, length 9 mm). Arrows indicate the build orientation.

2.4.2.1. Analysis of pore size and material strut size distribution. Binarized 3D image stacks were subjected to the Local Thickness Plugin for ImageJ (P. R. Dougherty and K-H. Kunzelmann; <http://www.optinav.com/imagej.html>). This plugin computes the local thickness of the 3D image stacks, defined as the diameter of the largest sphere that fits inside the pore and contains the voxel. The number of voxels with respective local thickness values and the corresponding pore diameter were used to calculate pore volume. The cumulative pore volume fraction was defined as the fraction of pores with a diameter larger than x μm among all pores, and its distribution was computed and represented as a line graph. The Local Thickness Plugin was also applied to the material (foreground) and material strut size distribution was computed.

2.4.2.2. Analysis of pore throat size distribution. Pore throat size was defined as the diameter of the largest sphere capable of reaching the pore from the outer surface. Pores with the respective pore throat size were detected by blocking the pore throats and tracing their interconnection from the outer surface as follows [23]. First, binarized 3D image stacks were subjected to the 3D Distance Map Plugin for ImageJ, one of the functions of the Local Thickness Plugin. This plugin assigned each background voxel a value representing the distance between the voxel and the border of the foreground. Pore throats for the corresponding radii were blocked by changing the background voxels of the corresponding distance map value to foreground voxels, thus blocking the pore throats. Subsequently, the volume of interconnected pores from the outer surface was measured and regarded as the volume of the pore for the corresponding pore throat size. The cumulative pore volume fraction distribution as a function of pore throat size was computed for each implant and represented as a line graph.

2.4.3. Observation using scanning electron microscopy

The surface of the implants was observed by field-emission scanning electron microscopy (SEM; Hitachi S-4300; Hitachi, Ltd., Tokyo, Japan). To observe the cross-section of the inner struts, each porous titanium plate was fractured using pliers. The cross-sectional area of the struts was also observed using SEM.

2.4.4. Assessment of mechanical properties

In accordance with ISO 13314:2011(E), mechanical testing was conducted. Porous cylinders (diameter: 12 mm; length: 12 mm, six cylinders of each type) were used for mechanical testing. Compressive testing was performed using a universal material testing machine (Model EHF-LV020K1-010; Shimadzu Corporation, Kyoto, Japan) at a crosshead speed of 1 mm/min. The elastic modulus was calculated from the slope of the compressive stress–strain curve in the linear elastic region, and the compressive yield strength was determined from the stress–strain curve using the 0.2% offset method.

2.5. In vivo experiments involving new bone formation in white rabbits

Two types of animal experiments were conducted in rabbits using porous-surfaced titanium plates or porous titanium cylinders. This animal study was approved by the Animal Research Committee of the Graduate School of Medicine, Kyoto University, Kyoto, Japan (Med Kyo 13242).

Before implantation, implants were conventionally sterilized using ethylene oxide gas. For detaching test, the porous titanium plates were implanted into the metaphysis of the tibia in mature male Japanese white rabbits weighing 2.8–3.2 kg. The surgical methods used have been described previously [32,33]. Briefly, using a dental burr, a 16×2 mm hole was made from the medial to the lateral cortex running parallel to the longitudinal axis of the tibial metaphysis. The plates were implanted in the frontal direction, perforating the tibia and protruding from the medial to the lateral cortex. The porous-surfaced side was placed at the front of the tibia. At 2, 4, or 8 weeks after implantation, rabbits were euthanized with an overdose of

intravenously administered pentobarbital. A total of 36 rabbits were used (eight plates of each type per implantation period). Eight samples were randomly divided into two groups: six samples for the measurement of detaching failure load and two samples for histological examination. The specimens for detaching tests were wrapped in wetted gauze, which was moistened with saline water at room temperature. Then, detaching tests were conducted as soon as possible after harvesting specimens.

For histological evaluation of bone ingrowth, the porous cylinders were implanted into the femoral condyle of mature male Japanese white rabbits. The surgical methods used have been described previously [15,28]. Briefly, a 6-mm diameter drill hole was made in the lateral femoral condyles. In this process, care was taken to avoid penetration of the medial femoral condyle. A porous titanium cylinder was implanted in this hole. At 2, 4, or 8 weeks after implantation, rabbits were euthanized. A total of 18 rabbits were used (four cylinders of each type per implantation period).

2.5.1. Detaching test with plate implants

The preparations for the detaching test [32] are shown in Fig. 3. Bone tissue surrounding the plates was removed with a dental burr so that no anterior bone segment was directly connected to a posterior bone segment. Using an Instron-type autograph (Model 1011; Aikoh Engineering Co., Ltd., Nagoya, Japan), traction was applied through hooks holding the anterior cortex and hooks holding the plate at a crosshead speed of 35 mm/min (Fig. 3). Care was taken so that strain was applied perpendicular to the surface of the implant. The load at which the plate became detached from the bone was recorded as the failure load. Six samples were analyzed for each type of implant for each implantation period. The remaining two samples were used for histological examination.

2.5.2. Histological examination

Two samples of plates and four samples of cylinders for each group at each implantation period were prepared for histological examination. Following euthanasia, the implant sites were harvested. The specimens were fixed in 10% phosphate-buffered formalin (pH 7.25) for 7 days and dehydrated in serial concentrations of ethanol (70, 80, 90, 99, 100, and 100% v/v) for 3 days per concentration. Specimens were then embedded in polyester resin. Thick sections (250 μm) were cut with a band saw (BS-3000CP; EXACT Cutting Systems, Norderstedt, Germany) perpendicular to the axis of the implant and ground to a thickness of 50–60 μm using a grinding–sliding machine (Microgrinding MG-4000; EXACT Cutting Systems). Each section was then stained with Stevenel's blue and Van Gieson's picrofuchsin [34], and purple, blue, and silver

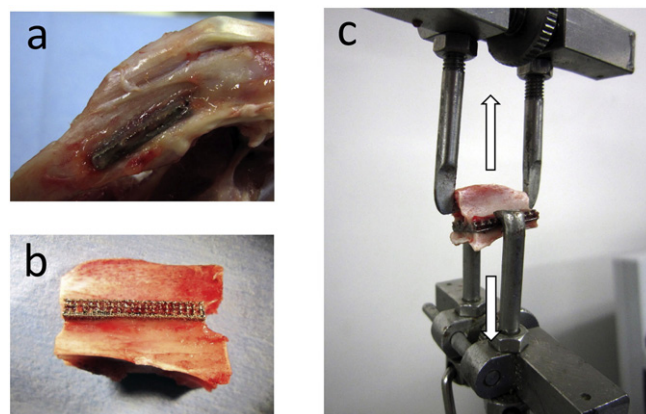


Fig. 3. The detaching test and prior preparation. a) Insertion of the titanium plate into the rabbit tibia. b) The bone–plate–bone construct after cutting the tibia at the proximal and distal ends of the plate. c) Tensile load was applied while holding the anterior cortex and the plate until detachment occurred.

indicate bone, soft tissue, and implants, respectively. Histological evaluation was performed on the stained sections using a digital microscope (DSX 500; Olympus Corporation, Tokyo, Japan).

2.5.3. Histomorphometry of porous cylinders

Using the frontal plane of porous cylinders, the depth of tissue ingrowth was measured. Fibrovascular tissue (FV), bone (B; woven or lamellar), and bone marrow-like tissue (BM) were distinguished according to images in previous literature [35]. FV was distinguished as tissue stained blue, which was composed of collagenous fibers, fibroblasts, blood vessels, and a few mononuclear cells. B was distinguished as tissue stained red, and immature bone with randomly oriented collagen as woven bone, and mature bone with a regular parallel alignment of collagen as lamellar bone. BM was distinguished as spongy tissue stained with blue which contained the fat, the bone marrow stromal cells, and blood systems cells.

Tissue differentiation in the pores of porous implants implanted in cancellous bone occurred as follows [23,35]:

- first stage: FV;
- second stage: FV with B (mainly woven);
- third stage: less BM in the pore (<50%) with FV and B (woven and lamellar);
- fourth stage: more BM in the pore (>50%) with B (mainly lamellar).

For each tissue differentiation stage (second: FV + B, third: BM + FV + B, or fourth: BM + B), the depth from the contact surface of the implant and maximum length within the implant were measured in each pore of the samples. Four samples were analyzed for each group after each implantation period.

2.6. Statistical analysis

All data are expressed as means \pm standard deviation (SD). All statistical analyses were performed using EZR (Saitama Medical Centre, Jichi Medical University, Saitama, Japan) [36], a graphical user interface for R (version 2.13.0; R Foundation for Statistical Computing, Vienna, Austria). One-way analysis of variance followed by *post-hoc* tests (Tukey–Kramer multiple comparison tests) were used to analyze bone-bonding ability and total tissue penetration length (i.e., the depth of FV + B from the surface of the implant) at each time point (2, 4, and 8 weeks) for the three different pore sizes. Differences of $P < 0.05$ were considered statistically significant.

3. Results

3.1. Porosity

We aimed for a porosity of 65% for the manufactured porous implants. Because the detailed configurations of the equipment influence the porosity of the manufactured implants, after several manufactures and adjustments of CAD and configurations, the porous implants used in this study were manufactured. Eventually, the porosity of the manufactured implants was 61.6% (SD = 0.4) for the P300 implant, 66.4% (SD = 0.3) for the P600 implant, and 64% (SD = 0.9) for the P900 implant (Table 1).

3.2. Microfocus X-ray computed tomography-based structural analysis

Images of the microstructures of the porous implants obtained via micro-CT revealed that the intended large pores (300, 600, and 900 μm) were accompanied by small pores (mainly 50–100 μm) produced as a result of the incomplete melting of the titanium powder (Fig. 4a–c). Following pore and pore throat size analysis, we were able to assign a color to pores according to their size and throat size.

Table 1

Porosity and microfocus X-ray computed tomography-based three-dimensional structural analysis.

| Group | Porosity (%) ^a | Pore size ^b | Pore throat size ^b | Material strut size ^b | Specific surface area (/mm) ^c |
|-------|---------------------------|------------------------|-------------------------------|----------------------------------|--|
| P300 | 61.6 \pm 0.4 | 309 \pm 84 | 274 \pm 67 | 220 \pm 47 | 6.09 |
| P600 | 66.4 \pm 0.3 | 632 \pm 171 | 573 \pm 147 | 416 \pm 134 | 4.38 |
| P900 | 64 \pm 0.9 | 956 \pm 202 | 821 \pm 170 | 577 \pm 234 | 2 |

^a Mean \pm standard deviation (SD; %), calculated from the weight and the apparent volume of the specimens.

^b Mean \pm SD (μm), calculated from the microfocus X-ray computed tomography (micro-CT) data.

^c Surface area and volume were calculated by micro-CT data of the specimens.

Representative figures are shown in Fig. 4d (pore size) and e (pore throat size).

The average pore sizes, average material strut sizes, and specific surface areas of each implant are shown in Table 1. The cumulative pore and interconnected pore volume fraction distributions are shown in Fig. 5. Eighty percent of the pores had a pore size between 240 and 420 μm for the P300 implant, between 570 and 840 μm for the P600 implant, and between 870 and 1200 μm for the P900 implant. Pore throat size distributions had a narrower range than pore sizes distributions. The pore size and pore throat size dissociations began at 240, 570, and 750 μm for the P300, P600, and P900 implants, respectively (arrows in Fig. 5). This implies that pores with a pore size greater than these values have narrower pore throats than their pore diameter; pore throat sizes were at least greater than these values.

3.3. Scanning electron microscopy observations

Fig. 6 shows SEM images of the implant surfaces after heat treatment at 1300 $^{\circ}\text{C}$ in an argon gas atmosphere. The surface appearances were similar between implants with different pore sizes. The particles that were loosely bonded to the surface after SLM were tightly bonded by sintering to the core part and provided remarkable irregularities in the surface. In terms of pore structure, in the P600 and P900 implants, pore shape was well controlled and the hexagonal shape of the original CAD was reproduced as a round shape in the two groups. Conversely, in the P300 implant, the pores were partially collapsed and the hexagonal shape of the CAD was reproduced as an ellipse.

Fig. 7 shows the fractured surface of the struts of the porous plate. It is observed that the central zone of the strut is perfectly melted, whereas the periphery is incompletely melted. It was difficult to measure the thickness of the incompletely melted layer accurately; however, it appeared similar in all specimens.

3.4. Results of mechanical testing

The elastic moduli of the P300, P600, and P900 implants were 557.4 (SD = 5.7), 648.9 (SD = 9.3), and 661.4 (SD = 13.2) MPa, respectively. The compressive yield strengths of the P300, P600, and P900 implants were 36.2 (SD = 1.3), 42 (SD = 1.4), and 51.4 (SD = 1) MPa, respectively. The stress–strain curves are shown in Fig. 8.

3.5. Implantation into rabbits

All rabbits tolerated the surgical procedure well. We observed no infection of the surgical site, dislocation of the implant, or adverse reactions such as inflammation or foreign body reaction on or around the implant.

3.5.1. Detaching test (failure load)

The detachment failure loads for each material at 2, 4, and 8 weeks after implantation are summarized in Fig. 9. At 2 weeks, the P600 implant demonstrated significantly high fixation strength (36.9 N) relative

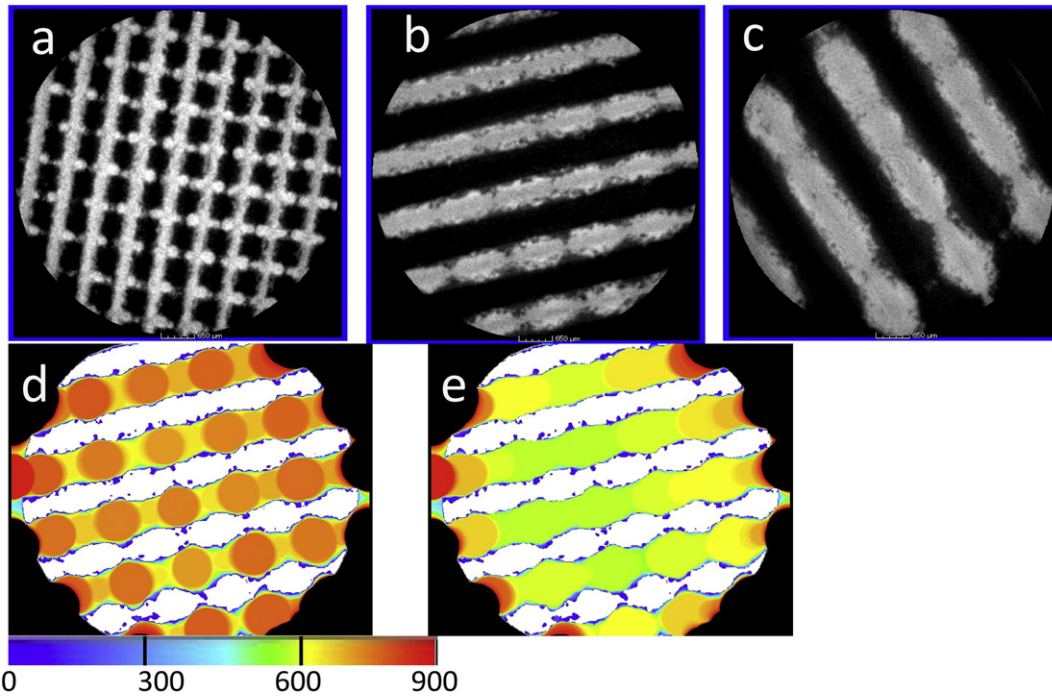


Fig. 4. Microfocus X-ray computed tomography images and structural analysis of each implant. a) P300, b) P600, and c) P900 implant designs. Pores in the P600 implant are colored in accordance with their pore size (d) and pore throat size (e). d) Deep pores colored yellow or orange have a pore size of between 600 and 800 μm . e) Deep pores colored green or yellow have a pore throat size between 500 and 600 μm .

to P300 and P900. At 4 and 8 weeks, failure always occurred at the anterior cortex where the samples were held by the equipment and the interface between bone and implant did not rupture. This indicates that the fixation strength of the implants at 4 and 8 weeks was too strong to be measured using this method.

3.5.2. Histological examination of plate implants

Histological images representative of each sample group are shown in Fig. 10 (at 2, 4, and 8 weeks), and high-magnification images around the bones and implants for each period are shown in Fig. 11.

At 2 weeks, new bone growth was observed in the peripheral pores of each implant.

At 4 weeks, new bone had grown into the pores. However, this bone tissue was mainly immature woven bone; well-remodeled lamellar bone was not observed. As shown at high magnification (Fig. 11) in the period from 2 to 4 weeks, new bone developed inside micropores on the surface and soft tissue was not observed between the bone and implant at 4 weeks. At 8 weeks, the new bone had been remodeled

into mature lamellar bone, and as a result, the continuity of the cortical bone had recovered. Marrow-like tissue was evident inside the porous implants.

3.5.3. Histological examination of porous cylinders

Histological images representative of each sample group are shown in Fig. 12. Tissue and bone ingrowth was observed in all groups. At 2 weeks, tissue migration occurred into the peripheral pores of the implants. At the front of the advanced tissue migration, undifferentiated fibrovascular tissue was observed and woven bone followed. At 4 and 8 weeks, following the advance of B (woven) containing FV, BM was present. The extent of tissue ingrowth is shown in Fig. 13. At 2 weeks, tissue differentiation with the P600 and P900 implants was superior to that of the P300 implants, although these differences were not statistically significant. At 4 weeks, the total tissue penetration length of the P900 implant was significantly higher than that of the P300 implant (Fig. 12).

4. Discussion

In this study, using *in-vivo* experiments, we investigated the optimal pore size of porous titanium implants manufactured by SLM. Three types of porous titanium implant (intended porosity of 65% and pore sizes of 300, 600, and 900 μm , designated the P300, P600, and P900 implants, respectively) were prepared. The porous structures of the implants were evaluated using micro-CT and confirmed to have an average pore size of 309, 632, and 956 μm , with pore throat size of at least 240, 570, and 750 μm , respectively (Table 1, Fig. 5). The P600 implant exhibited a significantly high bone–implant fixation ability at 2 weeks after implantation (Fig. 9). At 4 and 8 weeks, all types of porous titanium implant exhibited remarkably high fixation ability. In addition, after implantation into cancellous bone, bone ingrowth inside the P300 implant at 4 weeks was significantly lower than that of the P900 implant (Fig. 13).

Many studies have examined the influence of porosity and pore shape of porous materials on biological behavior using calcium phosphate. The majority of these studies focused on a pore size less than

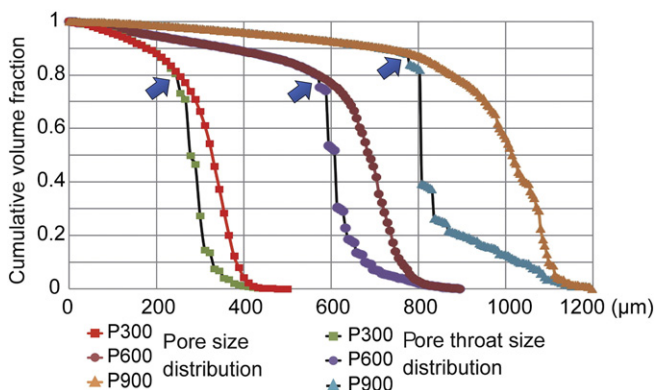


Fig. 5. Three-dimensional pore size and pore throat size distributions in each implant.

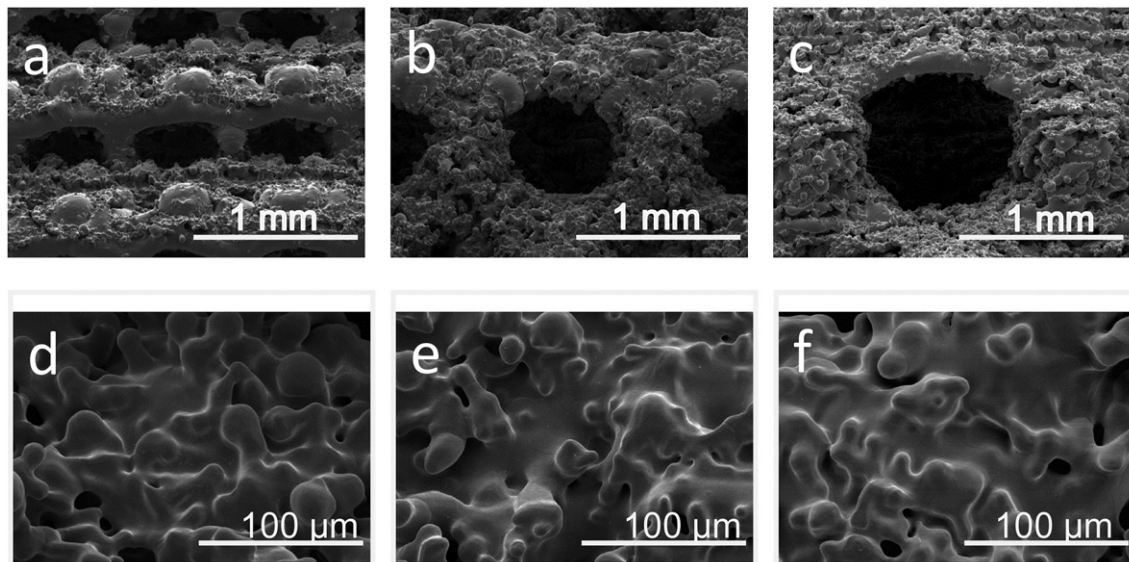


Fig. 6. Scanning electron microscopy images of porous-surfaced titanium plates with different pore sizes. a) P300, b) P600, and c) P900. d–f) magnified images of a–c, respectively. These views were observed from 35° oblique direction to the build orientation.

200 μm [37,38]. This is mainly because porous calcium phosphate implants with both high porosity and large pore size have proven difficult to manufacture in the past. In addition, these studies recommend high porosity and large pore size to achieve good bone ingrowth for reasons related to vascularization and cell size. Similar results were obtained using porous titanium produced by conventional methods. Porous titanium produced by 3D fiber deposition (with pore sizes of 160, 400, and 680 μm and varying porosity) were examined in goats by Li et al. [24]. They concluded that increased pore size and porosity induces greater bone formation. Likewise, in porous titanium produced using the powder sintering method, big pores (500–1500 μm) were reported to

initiate greater bone formation than small pores (250–500 μm) in the rabbit femur [23]. However, to accurately evaluate the effect of pore size, other parameters, such as porosity, interconnectivity, mechanical properties, and surface characteristics, must be kept identical. The scaffolds used in these studies had poorly controlled architecture and wide pore size distribution. Therefore, it is difficult to discern the true effect of pore size from these studies.

AM is suited to the manufacture of porous titanium implants with a precisely controlled pore size, porosity, and interconnectivity. However, no reports compare implants of different pore sizes with a constant porosity manufactured using AM, and the effect of a small pore size of

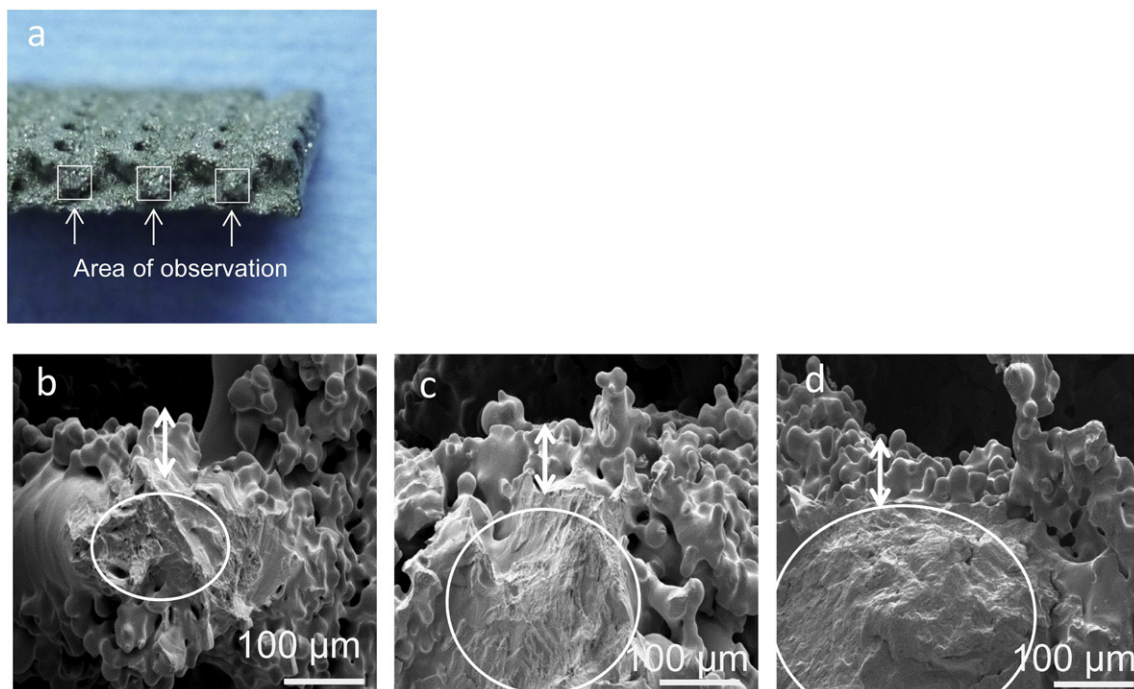


Fig. 7. Scanning electron microscopy images of the cross section of the inner strut of porous titanium-surfaced plates with different pore sizes. Each plate was fractured using pliers. a) The representative appearance of the fractured surface. Square: area observed by scanning electron microscopy. b) P300, c) P600, d) P900. Circle: completely melted area; arrow: incompletely melted area.

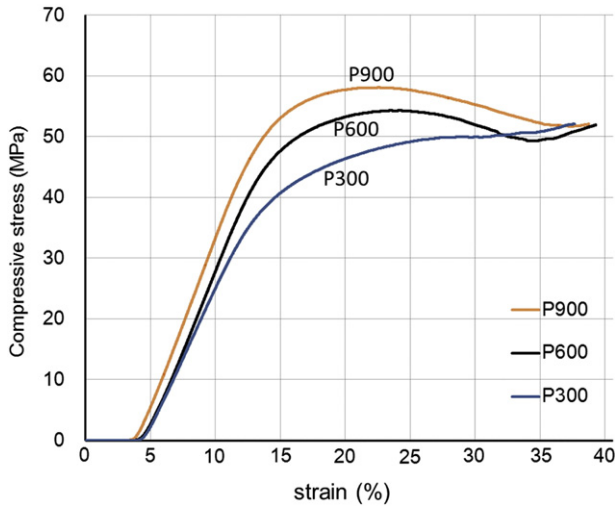


Fig. 8. Typical stress–strain curves of porous cylinders with different pore sizes.

approximately 300 μm has not yet been examined *in vivo*. In this regard, our study is the first to demonstrate the independent effect of pore size with a constant porosity; i.e., the superiority of a porous implant with a pore size of 600 μm to implants with a pore size of 300 or 900 μm.

Bone ingrowth into the pores of cylindrical titanium implants inserted into cancellous bone was lower in the P300 implant than in the P600 and P900 implants. This can be explained by vascularization that is essential for bone formation. Bai et al. [39] reported that an increase in pore size resulted in an increase in the size of blood vessels formed; however, there was no marked increase in extent of vascularization with a pore size above 400 μm. Based on these findings, the P600 and P900 implants are more advantageous in terms of vascularization than the P300 implant. On the other hand, a higher average curvature is reported to induce higher tissue amplification *in vitro* [40,41]. If the same structure is used with a different pore size, the cross sectional shape is the same, but the average curvature of the pore becomes higher in inverse proportion to pore size [40,42]. With respect to curvature, smaller pores offer an advantage. Considering these factors, the inferiority of the P300 implant to the P600 and P900 implants in bone ingrowth is mainly due to the greater negative effect of vascularization than the positive effect of curvature. Our finding that bone ingrowth of the P600 implant tends to be higher than that of the P900 implant at 2 weeks may be explained mainly by the positive effect of a higher curvature.

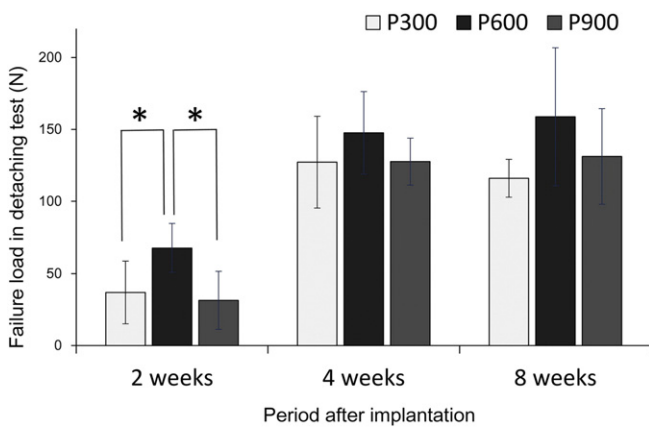


Fig. 9. Failure load (N) in the detaching test of porous-surfaced titanium plates with different pore sizes after implantation for different periods. Error bar: standard deviation. * $P < 0.05$.

In addition to vascularization and curvature, with respect to fixation ability, specific surface area is another essential factor. Increased specific surface area is considered to have a positive effect on bone–implant fixation ability [43]. The specific surface area of the P300 implant was larger than that of the P600 and P900 implants (Table 1), although they have the same surface characteristics. Therefore, if pore size had no effect on fixation ability, the P300 implant may have shown the highest fixation ability. However, in this examination, the P600 implant exhibited a significantly higher bone–implant fixation strength than the P300 and P900 implants at 2 weeks (Fig. 9). The inferiority of the P300 implant to the P600 implant in bone-bonding ability may be explained by the greater effect of reduced vascularization than the positive effect of increased surface area and curvature. The superiority of the P600 to the P900 implant in bone-bonding ability may be due to the increased surface area and favorable curvature for bone tissue amplification discussed above. At 4 and 8 weeks, all types of porous titanium implant exhibited a remarkably high fixation strength and there were no statistical differences between them. Histologically, both bone ingrowth into the deep pores of the implant and bone ingrowth very close to the implant surface were observed (Figs. 10 and 11). These findings indicated the tight mechanical interlocking of implant and bone.

Because the current detaching test is simple and the results are consistent, we can compare the fixation strength observed in this study with previously reported data on the modification of surface topography. In recent work using the same model, Kawai et al. [44] evaluated the arc-sprayed rough surface of titanium metal and reported that its fixation strength is 65.4 N at 4 weeks [44]. Our data is superior to these previously reported data and indicate that porous titanium manufactured by SLM is advantageous for implants that demand high fixation ability. In contrast, the high fixation ability of porous metal in this study was too high to be measured using this method at 4 and 8 weeks. Other methods, such as the push-out test [45], should be conducted.

At 8 weeks, new bone in the pores of titanium plates remodeled into mature cortical bone and eventually cortical continuity was recovered (Fig. 10). Furthermore, in porous cylinders, marrow-like tissue spread deeply (Fig. 13). These findings indicate that the restoration of bone and soft tissue was not prevented in the pores. Good interconnectivity and well-controlled pore throat size is essential for vascular tissue ingrowth and bone conductivity, which led to the restoration of bone and soft tissue [23,39]. Our porous implants have well-interconnected pores and well-controlled pore throat size (Fig. 5, Table 1), confirmed by 3D micro-CT-based analysis. Conventional methods to produce porous implants risk scattering the interconnectivity, which can cause partial deficits in bone ingrowth. Well-controlled interconnectivity is a peculiarity of AM, and porous implants manufactured by AM have this further advantage.

With respect to the basic structure, the diamond crystal lattice with hexagonal pore throat shape was adopted because of its ease of manufacturing and mechanical stability under multidirectional forces. Under *in vitro* examination, tissue amplification was reported to be greater for the hexagonal shape than for square and triangular shapes [26,40]. This finding suggests that the diamond crystal lattice may show a superior tissue amplification relative to other structures.

The porous titanium used here has compressive yield strength of around 50 MPa, which is smaller than that of cortical bone (80–120 MPa). The elastic modulus of each implant (557–661 MPa) is much lower than that of cortical bone (17 GPa) [46] and close to that of human trabecular bone (689 MPa) [47]. We conclude that the mechanical property used here is suited for use under load-bearing conditions and for prevention of stress shielding. Mechanical properties of porous scaffolds result in altered mechanical loading [48] and bone regeneration under load-bearing conditions [42]. Because the animal model used here was investigated under non-load-bearing conditions, the difference in compressive yield strength may have exerted only a small influence. However, load-bearing conditions may have yielded

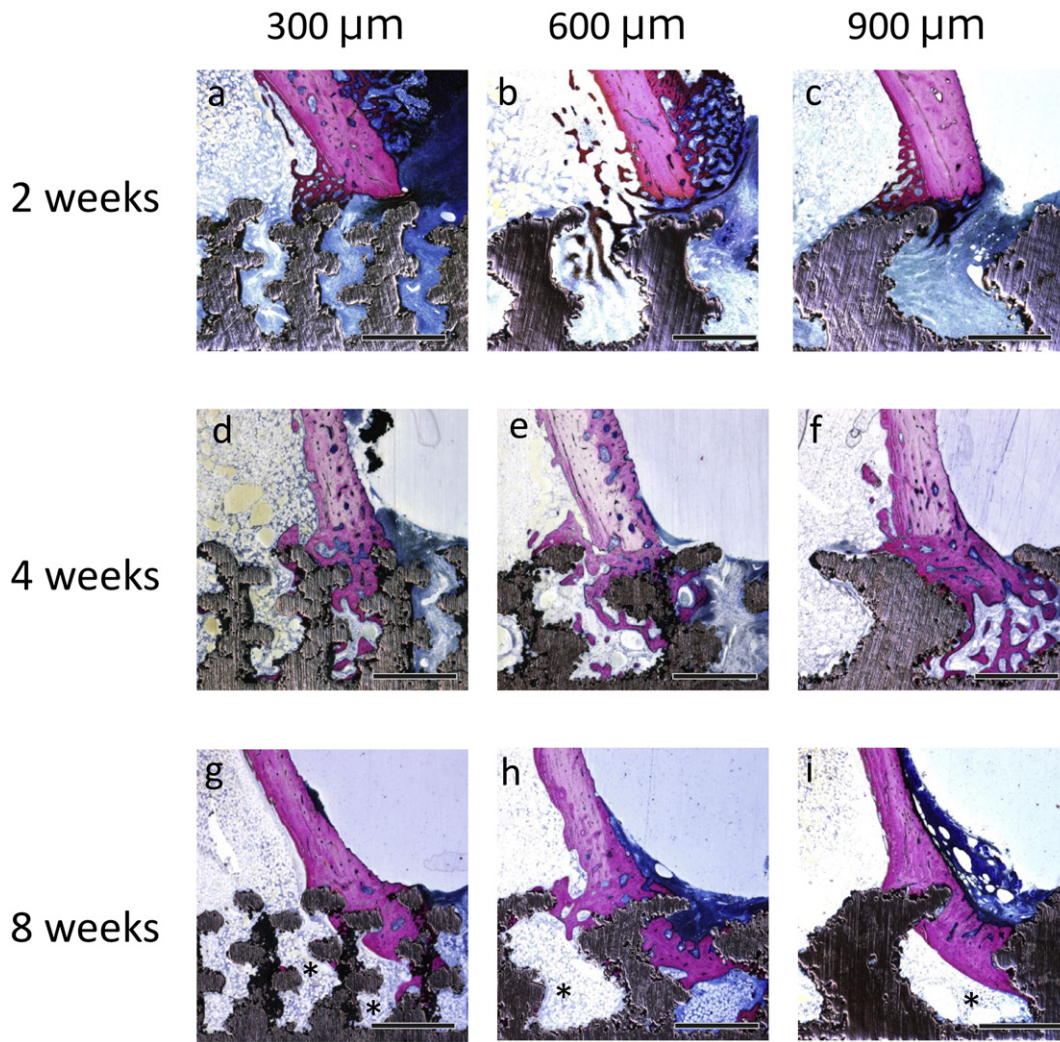


Fig. 10. Non-decalcified histologic sections of porous-surfaced titanium plates implanted into rabbit tibia. Stain: Stevenel's blue and Van Gieson's picrofuchsin. Purple indicates bone; silver indicates the titanium implant. *: marrow-like tissue spreading into porous area. Scale bars: 1 mm.

slightly different results. Further study under load-bearing conditions will be necessary to confirm the results of this study.

To clarify why the compressive strength of the P300 implant was low, we examined the cross-section of the inner strut of plates fractured using pliers. As shown in Fig. 7, the complete melting area in the strut was remarkably low in the P300 implant because the thickness of the

incompletely melted area was almost identical in all implants. This may explain the lower compressive strength of the P300 implants. Compressive stress is strongly associated with the basic structure and size of struts [49,50], and AM is advantageous in that it can change these parameters. Therefore, the compressive strength of implants manufactured by AM can be increased according to individual

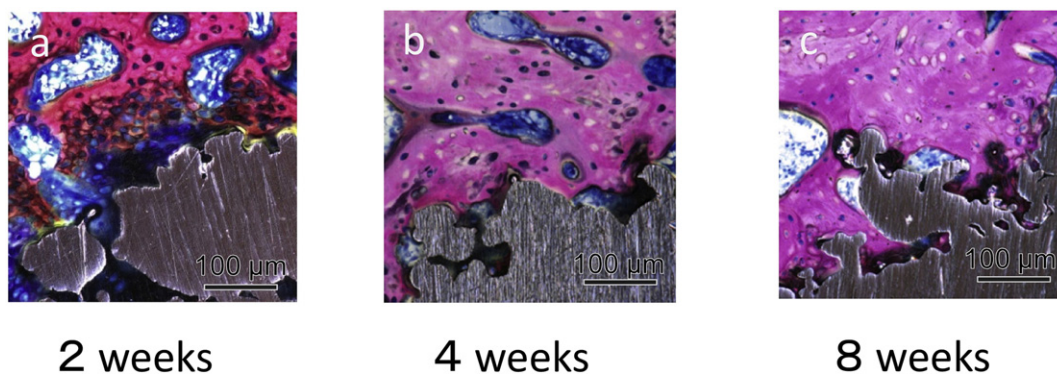


Fig. 11. High-magnification images of non-decalcified histologic sections of porous-surfaced titanium plants implanted into rabbit tibia. Stain: Stevenel's blue and Van Gieson's picrofuchsin.

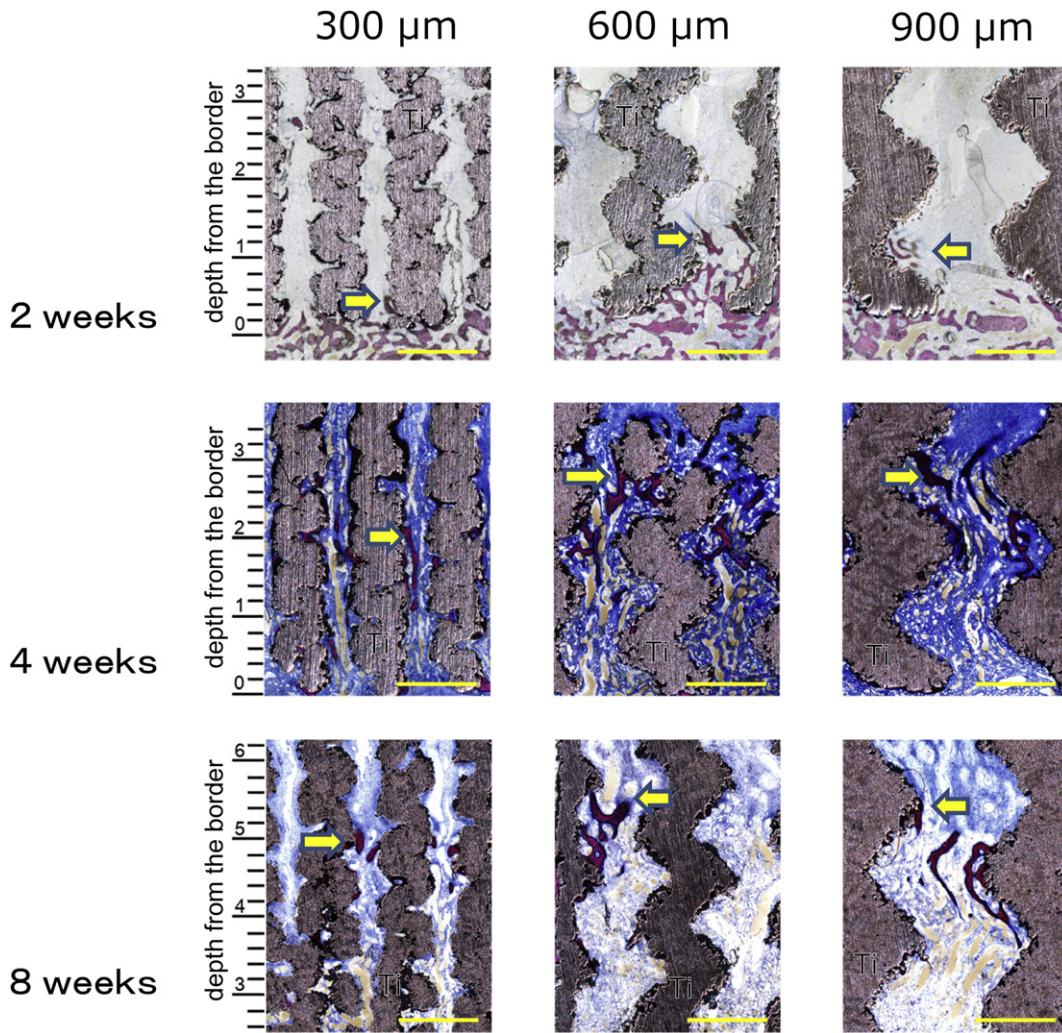


Fig. 12. Non-decalcified histologic sections of cylindrical porous titanium implants implanted into rabbit tibia. The reference for the scale cited at the left-hand edge of each image is the interface between the porous structure and the bone. Stain: Stevenel's blue and Van Gieson's picrofuchsin. Arrow: bone. Ti: porous titanium. Purple indicates bone; silver indicates the titanium implant. Scale bar: 1 mm.

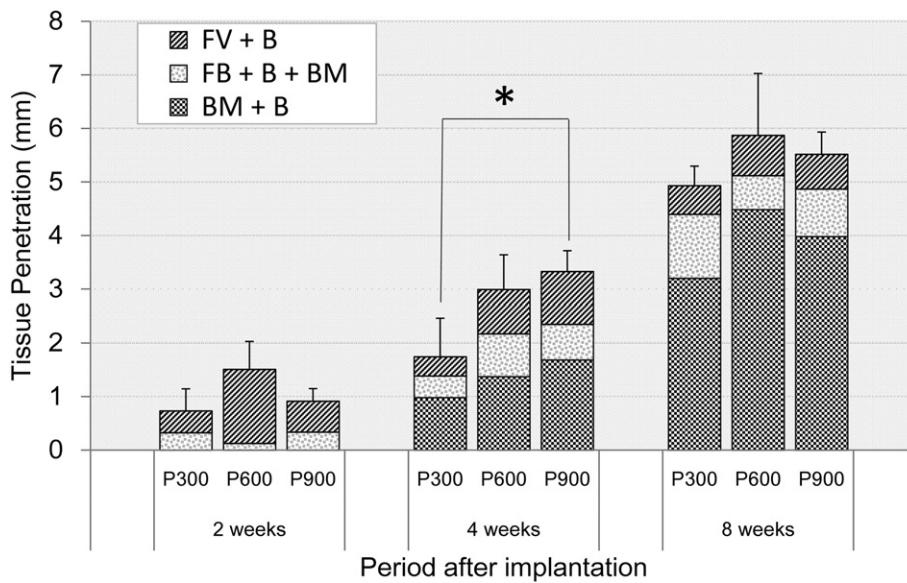


Fig. 13. Schematic drawing of tissue ingrowth into cylindrical porous titanium implants implanted into rabbit femurs. FB + B: fibrous tissue with bone (mainly woven); FB + B + BM: less bone marrow-like tissue in the pore (<50%) with fibrous tissue and bone (woven and lamella); BM + B: more bone marrow-like tissue in the pore (>50%) and bone (mainly lamella). All values shown are averages. Error bar: standard deviation of FB + B. *P < 0.05.

situations. Moreover, porous titanium is unresorbable, which ensures its long-term stability even under load-bearing conditions in contrast to conventional bone substitutes composed of calcium phosphate.

With respect to the orthopedic load-bearing implant, one of the most essential factors is sufficient mechanical strength to resist handling during implantation and *in-vivo* loading. Thus, the porous structure of P600 with a compressive yield strength of 42 MPa can be applied to the surface of a cementless prosthesis or bone substitute for load-bearing conditions. In certain conditions, such as spinal vertebral body replacement, for which the compressive yield strength of 42 MPa is insufficient [28], additional supportive structures may be necessary. Nevertheless, the mechanical properties and the results of *in-vivo* study encourage us to use the P600 structure as a basic structure of such an orthopedic application. Moreover, using the P600 implant as a template, both readymade implants, which have a seamless porous surface and bulk, and implants with a customized shape based on individual demands can be manufactured by AM.

Some limitations of this study should be acknowledged. The first limitation relates to the restrictions of manufacture. The minimum strut or wall size of objects manufactured by SLM is restricted by several factors, including laser spot size, laser power, scanning speed, particle size of Ti metal, and the effect of thermal conductivity around the material [14,51,52]. Therefore, we are currently unable to investigate the effects of a pore size smaller than 300 μm . Moreover, the pore shape was partially collapsed, and the porosity was not perfectly uniform. These differences may have affected the results. Particularly, the fact that the P600 implant has the highest porosity may account for its superiority. However, compared with the difference in pore size (309–956 μm) and surface area, the difference in porosity (61.6–66.4%) is relatively small. Therefore, we believe that the difference in porosity had only a small effect on the results of our animal experiments. Rather, we believe that the differences in pore size and surface area had a much greater influence on the results of our animal experiments. In future, with advances in the equipment, it may be possible to manufacture and examine smaller-sized or more precise pores. Second, the examination was conducted under restricted conditions. The basic structure was diamond lattice. Using another basic structure, the optimal pore size may be slightly different. Furthermore, electron beam melting (EBM), another AM technique, produces a different surface roughness compared with that produced by SLM [53]. When EBM is used, the optimal structure may be slightly different. Third, this study was conducted in animals under non-load-bearing conditions. The optimal pore size for humans under load-bearing conditions may be slightly different; thus, further study is warranted in future.

5. Conclusion

In this study, we manufactured a well-controlled scaffold using SLM and investigated the effect of pore size on bone ingrowth in rabbits. Porous titanium implants with a pore size of 600 μm (P600) showed significantly higher fixation ability than those with a pore size of 300 μm (P300) and 900 μm (P900), and the P300 implant exhibited inferior bone ingrowth in cancellous bone compared with that of the P600 and P900 implants. Because of the appropriate compressive strength, high fixation ability in the early period, and deep bone ingrowth of the P600 implant, it represents a good candidate for the surface structure of joint prostheses, spinal fusion devices, and other custom-made bone substitutes.

Financial support and role of the sponsor

This study was supported by a Grant in Aid for Scientific Research from the Japan Society for the Promotion of Science (No. 21560720).

Conflict of interest

No benefits in any form have been or will be received from a commercial party related directly or indirectly to the subject of this manuscript.

Acknowledgments

The authors thank Keita Ishimizu of Kyocera Medical Corporation, Osaka, Japan, for designing the porous titanium implants.

References

- [1] W.C. Head, D.J. Bauk, R.H. Emerson Jr., *Clin. Orthop. Relat. Res.* (1995) 85–90.
- [2] R.M. Pilliar, *Clin. Orthop. Relat. Res.* (1976) (1983) 42–51.
- [3] S.A. Hacking, J.D. Bobyn, M. Tanzer, J.J. Krygier, *Clin. Orthop. Relat. Res.* (1999) 240–253.
- [4] K.A. Zweymuller, F.K. Lintner, M.F. Semlitsch, *Clin. Orthop. Relat. Res.* (1988) 195–206.
- [5] M. Jasty, C.R. Bragdon, T. Haire, R.D. Mulroy Jr., W.H. Harris, *J. Biomed. Mater. Res.* 27 (1993) 639–644.
- [6] G. Ryan, A. Pandit, D.P. Apatsidis, *Biomaterials* 27 (2006) 2651–2670.
- [7] I.H. Oh, N. Nomura, N. Masahashi, S. Hanada, *Scr. Mater.* 49 (2003) 1197–1202.
- [8] C.E. Wen, Y. Yamada, K. Shimojima, Y. Chino, H. Hosokawa, M. Mabuchi, *J. Mater. Res.* 17 (2002) 2633–2639.
- [9] N.G. Davis, J. Teisen, C. Schuh, D.C. Dunand, *J. Mater. Res.* 16 (2001) 1508–1519.
- [10] J.W.M. Vehof, P.H.M. Spauwen, J.A. Jansen, *Biomaterials* 21 (2000) 2003–2009.
- [11] J.P. Li, S.H. Li, K. De Groot, P. Layrolle, *Key Eng. Mater.* (2002) 51–54.
- [12] J.P. Kruth, L. Froyen, J. Van Vaerenbergh, P. Mercelis, M. Rombouts, B. Lauwers, *J. Mater. Process. Technol.* 149 (2004) 616–622.
- [13] M. Agarwala, D. Bourell, J. Beaman, H. Marcus, J. Barlow, *Rapid Prototyp. J.* 1 (1995) 26–36.
- [14] J.P. Kruth, P. Mercelis, J. Van Vaerenbergh, L. Froyen, M. Rombouts, *Rapid Prototyp. J.* 11 (2005) 26–36.
- [15] D.K. Pattanayak, A. Fukuda, T. Matsushita, M. Takemoto, S. Fujibayashi, K. Sasaki, N. Nishida, T. Nakamura, T. Kokubo, *Acta Biomater.* 7 (2011) 1398–1406.
- [16] L.E. Murr, S.A. Quinones, S.M. Gaytan, M.I. Lopez, A. Rodela, E.Y. Martinez, D.H. Hernandez, E. Martinez, F. Medina, R.B. Wicker, *J. Mech. Behav. Biomed. Mater.* 2 (2009) 20–32.
- [17] Y. Li, W. Yang, X. Li, X. Zhang, C. Wang, X. Meng, Y. Pei, X. Fan, P. Lan, C. Wang, X. Li, Z. Guo, *ACS Appl. Mater. Interfaces* 7 (2015) 5715–5724.
- [18] J. Yang, H. Cai, Z.J. Liu, K. Zhang, H. Leng, C. Sun, Z. Wang, J. Lv, *Spine* (2014).
- [19] S.H. Wu, Y. Li, Y.Q. Zhang, X.K. Li, C.F. Yuan, Y.L. Hao, Z.Y. Zhang, Z. Guo, *Artif. Organs* 37 (2013) E191–E201.
- [20] V. Karageorgiou, D. Kaplan, *Biomaterials* 26 (2005) 5474–5491.
- [21] S.V. Dorozhkin, *Biomaterials* 31 (2010) 1465–1485.
- [22] M. Bohner, F. Baumgart, *Biomaterials* 25 (2004) 3569–3582.
- [23] B. Otsuki, M. Takemoto, S. Fujibayashi, M. Neo, T. Kokubo, T. Nakamura, *Biomaterials* 27 (2006) 5892–5900.
- [24] J.P. Li, P. Habibovic, M. van den Doel, C.E. Wilson, J.R. de Wijn, C.A. van Blitterswijk, K. de Groot, *Biomaterials* 28 (2007) 2810–2820.
- [25] A.P. Rubshtein, I.S. Trakhtenberg, E.B. Makarova, E.B. Triphonova, D.G. Bliznets, L.I. Yakovenkova, A.B. Vladimirov, *Mater. Sci. Eng. C* 35 (2014) 363–369.
- [26] S. Van Bael, Y.C. Chai, S. Truscello, M. Moesen, G. Kerckhofs, H. Van Oosterwyck, J.P. Kruth, J. Schrooten, *Acta Biomater.* 8 (2012) 2824–2834.
- [27] J. Van Der Stok, O.P. Van Der Jagt, S. Amin Yavari, M.F.P. De Haas, J.H. Waarsing, H. Jahr, E.M.M. Van Lieshout, P. Patka, J.A.N. Verhaar, A.A. Zadpoor, H. Weinans, *J. Orthop. Res.* 31 (2013) 792–799.
- [28] M. Takemoto, S. Fujibayashi, M. Neo, J. Suzuki, T. Kokubo, T. Nakamura, *Biomaterials* 26 (2005) 6014–6023.
- [29] R. Tubino, L. Piseri, G. Zerbi, *J. Chem. Phys.* 56 (1972) 1022–1039.
- [30] T.M.D.K. Pattanayak, H. Takadama, A. Fukuda, M. Takemoto, S. Fujibayashi, K. Sasaki, N. Nishida, T. Nakamura, T. Kokubo, *Bioceram. Dev. Appl.* 1 (2011) 3.
- [31] H. Akiyama, T. Morishima, M. Takemoto, K. Yamamoto, H. Otsuka, T. Iwase, T. Kabata, T. Soeda, K. Kawanabe, K. Sato, T. Nakamura, *J. Orthop. Sci.* 16 (2011) 26–37.
- [32] T. Nakamura, T. Yamamuro, S. Higashi, T. Kokubo, S. Ito, *J. Biomed. Mater. Res.* 19 (1985) 685–698.
- [33] S. Fujibayashi, T. Nakamura, S. Nishiguchi, J. Tamura, M. Uchida, H.M. Kim, T. Kokubo, *J. Biomed. Mater. Res.* 56 (2001) 562–570.
- [34] C. Maniopoulos, A. Rodriguez, D.A. Deporter, A.H. Melcher, *Int. J. Oral Maxillofac. Implants* 1 (1986) 31–37.
- [35] M.B. Pabbruwe, O.C. Standard, C.C. Sorrell, C.R. Howlett, *J. Biomed. Mater. Res. Part A* 68 (2004) 305–313.
- [36] Y. Kanda, *Bone Marrow Transplant.* 48 (2013) 452–458.
- [37] A.I. Itli, H.O. Ylnen, C. Ekholm, K.H. Karlsson, H.T. Aro, *J. Biomed. Mater. Res.* 58 (2001) 679–683.
- [38] Y.S. Chang, H.O. Gu, M. Kobayashi, M. Oka, *J. Arthroplast.* 13 (1998) 816–825.
- [39] F. Bai, Z. Wang, J. Lu, J. Liu, G. Chen, R. Lv, J. Wang, K. Lin, J. Zhang, X. Huang, *Tissue Eng. Part A* 16 (2010) 3791–3803.
- [40] M. Rumpler, A. Woesz, J.W.C. Dunlop, J.T. Van Dongen, P. Fratzl, *J. R. Soc. Interface* 5 (2008) 1173–1180.

- [41] J. Knychala, N. Bouropoulos, C.J. Catt, O.L. Katsamenis, C.P. Please, B.G. Sengers, *Ann. Biomed. Eng.* 41 (2013) 917–930.
- [42] A.A. Zadpoor, *Biomater. Sci.* 3 (2015) 231–245.
- [43] H. Kienapfel, C. Sprey, A. Wilke, P. Griss, *J. Arthroplast.* 14 (1999) 355–368.
- [44] T. Kawai, M. Takemoto, S. Fujibayashi, M. Tanaka, H. Akiyama, T. Nakamura, S. Matsuda, *J. Biomed. Mater. Res. Part B, Appl. Biomater.* (2014).
- [45] N. Chandra, H. Ghonem, *Compos. A: Appl. Sci. Manuf.* 32 (2001) 575–584.
- [46] X.N. Dong, X.E. Guo, *J. Biomech.* 37 (2004) 1281–1287.
- [47] A. Odgaard, F. Linde, *J. Biomech.* 24 (1991) 691–698.
- [48] S. Amin Yavari, J. van der Stok, S.M. Ahmadi, R. Wauthle, J. Schrooten, H. Weinans, A.A. Zadpoor, *J. Biomech.* 47 (2014) 2700–2708.
- [49] N.W. Hrabec, P. Heintl, B. Flinn, C. Körner, R.K. Bordia, *J. Biomed. Mater. Res. Part B Appl. Biomater.* 99B (2011) 313–320.
- [50] P. Heintl, L. Müller, C. Körner, R.F. Singer, F.A. Müller, *Acta Biomater.* 4 (2008) 1536–1544.
- [51] B. Vandenbroucke, J. Kruth, *Rapid Prototyp. J.* 13 (2007) 196–203.
- [52] D.A. Hollander, M. Von Walter, T. Wirtz, R. Sellei, B. Schmidt-Rohlfing, O. Paar, H.J. Erli, *Biomaterials* 27 (2006) 955–963.
- [53] J.E. Biemond, G. Hannink, N. Verdonschot, P. Buma, *J. Mater. Sci. Mater. Med.* 24 (2013) 745–753.